Journal of Sound and Vibration (2000) **234**(5), 777–798
doi:10.1006/jsvi.1999.3183, available online at http://www.idealibrary.com on IDEAL®

THE TRANSMISSION CHARACTERISTICS OF THE ELASTIC SHEAR WAVE AT A SEMI-INFINITE EFFECTIVE CHIRAL MEDIUM

SHIUH-KUANG YANG AND SHAO-YI HSIA

Department of Mechanical Engineering, National Sun Yat-Sen University, Kaohsiung, Taiwan, Republic of China. E-mail: skyang@mail.nsysu.edu.tw

(*Received* 8 *November* 1996, *and in final form* 23 *December* 1999)

The plane wave propagating in effective chiral (isotropic, non-centrosymmetric) materials had been asymptotically investigated. They can be constructed by embedding structural chiral microstructures in a host medium, and six independent wavenumbers can hence be observed from the dispersion equations. Two of the wavenumbers represent the non-dispersive longitudinal waves while the remaining four represent the dispersive circularly polarized shear waves. The dispersion equations also indicate that two transition frequencies divide the frequency spectrum of the transverse wavenumbers into three different groups and the four transverse mode can only be distinguished in a specified frequency range. To continue our previous research, the field equations governing the harmonic motions at the achiral–chiral interface are written as a matrix form to solve the reflected and transmitted wave fields. Numerical results show that the P-, SV-, and SH-waves are coupled together when an elastic shear wave is incident at the achiral–chiral interface. Meanwhile, the two coupled transverse waves, i.e., the LCP and RCP plane waves, will degenerate to a linearly transverse plane wave when the shear wave is incident normally. The phenomenon may explain why the mode conversion due to the chirality is particularly enhanced between the first and second transition frequencies.

1. INTRODUCTION

Chiral media, due to the lack of geometric symmetry between an object and its mirror image, have long been known in optics under the more common name of optically active materials. They are characterized by an intrinsic left- or right-handedness at optical frequencies, due to a helical natural structure, and hence cannot be made to coincide with the object itself by any operation involving rotations and/or translations. Therefore, waves of different circular polarization propagate in these media at different phase velocities. As a result, a linearly polarized electromagnetic wave incident at a chiral medium emerges with its plane of polarization rotated about its direction of propagation [1].

Since the electromagnetic waves can discriminate the chirality of objects, there is no reason that other transverse waves cannot do so. In general, the fields in elastic solid consist of both transverse and longitudinal components, and therefore an elastic wave should be able to sense the chirality also. Because of this, the wave field of the structural chiral media and the effective chiral materials had been asymptotically investigated [2–4]. The linear theory for non-centrosymmetric, isotropic (hemitropic) micropolar media or mechanical active solids was developed by Aero and Kuvshinskii [5] Erigen [6] and Nowacki [7]. They reported that the continuum is composed of randomly arranged springs, is isotropic

0022-460X/00/300777 + 22 $35.00/0

concerning any proper orthogonal transformations but not with respect to reflections, and hence the microstructure possesses a screw-like property, or a handedness. Such a medium undergoing a homogeneous deformation can support couple stresses and spin inertia. Therefore, micropolar solution in solid mechanics results in both the displacement field and the orientational field. From our previous work [2], it is known that an effective chiral medium can be constructed by embedding structural chiral microstructures in a host matrix. Such a material is mirror asymmetric or chiral; therefore, six independent wavenumbers are possible. Two of the wavenumbers represent non-dispersive longitudinal fields, while the remaining four are dispersive circularly polarized transverse fields. Meanwhile, the dispersion equations of the transverse field also indicate that two transition frequencies divide the frequency response of the transverse wavenumbers into three different groups, and hence the four transverse modes can only be distinguished in a specified frequency range. Thus, the microstructural size of the effective chiral material will be sufficiently large compared to the transverse wavelength so that an incident elastic shear wave can sense its chirality, while the microstructural size could be adequately small so that the material is effectively chiral.

The subject of reflection and transmission of plane waves at an interface between two semi-infinite media, in welded contact, has been discussed by various authors [8–12]. The reflection of plane wave from the flat boundary of micropolar elastic half-space was discussed by Parfitt and Eringen [8] in 1969. Then Tomar and Gogna extended the investigation to a longitudinal microrotational wave [9] and a longitudinal displacement wave [10] impinging at a plane discontinuity between two micropolar elastic solids in welded contact. Simultaneously, Lakhtakia *et al.* [11, 12] presented a nice theoretical model concerning the reflection phenomena when an incident plane wave is propagating at the interface between the elastic solid and the chiral material. To continue our previous research, this paper studies the propagation of elastic transverse waves at the achiral–chiral boundary. It should be noted that although this paper deals with a similar problem related to reference [11], the following contributions can be found in this paper:

1. The dispersion equations indicate that two transition frequencies divided the frequency spectrum of the transverse wavenumbers into three different groups and the four transverse modes can only be distinguished in a specific frequency range (Figure 1). This unique result may explain why the microstructural size of the effective chiral material should be sufficiently large compared to the transverse wavelength so that an incident elastic plane wave can sense its chirality while the microstructural size could be adequately small so that the material is effective chiral. Therefore, our numerical analysis concentrates on the phenomenon of the two transition frequencies found only in our previous work. The results obtained in this paper are useful in designing and fabrication the effective chiral samples.
2. The material constants used in our paper are different from those used in reference [11]. In reference [11], the acoustic impedance Z is given as $Z = \rho C_L = \rho \times \sqrt{(\lambda + 2\mu)/\rho} = 1200 \times 95742 = 1{\cdot}14 \times 10^6\ \mathrm{kg/s\,m^2}$, where λ and μ are *Lame*' constants. This value is close to that for water. However, the Poisson's ratio ($v = \lambda/2(\lambda + \mu) = 0{\cdot}31$) indicates that this is a hard material. Thus, the material is too hard to be used as an anechoic coating. For the applications in anechoic coating, the composite may be fabricated by embedding the helical arrangement of microstructures, for instance, the structural chiral inclusions or springs, in the soft matrix (such as soft rubber used in many practical applications). To ensure that the chiral effect can be found in the samples, we proposed a hypothesis about the material constants to characterize the effective chiral composites in references [2, 4].

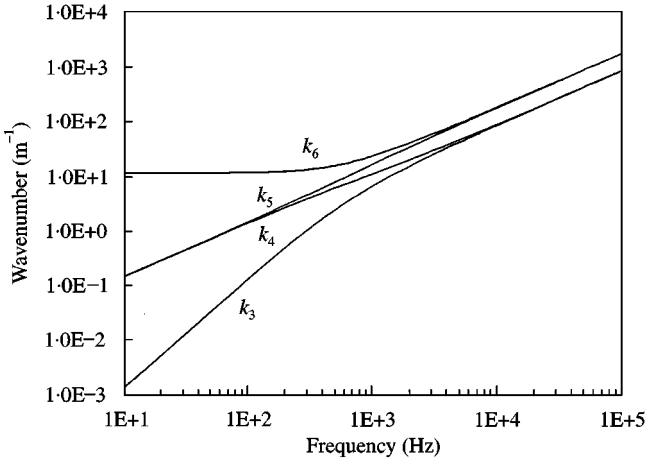

Figure 1. The wavenumbers as functions of the frequency [2]. The material moduli are listed in Table 1.

TABLE 1

The material constants for the isotropic elastic solid and the chiral solid

Isotropic elastic solid [13]	Chiral solid [2, 4]
$\rho_1 = 970\ \text{kg/m}^3$	$\rho_2 = 1012\ \text{kg/m}^3$
$\lambda_1 = 1343{\cdot}8\ \text{MPa}$	$\lambda_2 = 2124{\cdot}7\ \text{MPa}$
$\mu_1 = 61{\cdot}8\ \text{MPa}$	$\mu_2 = 204\ \text{MPa}$
	$\alpha = 3 \times 10^6\ \text{N}$
	$\beta = 3 \times 10^6\ \text{N}$
	$\gamma = 4 \times 10^6\ \text{N}$
	$C_3 = 16 \times 10^6\ \text{N/m}$
	$J = 0{\cdot}01\ \text{m}^2$

Considering the general composite theory and the non-negative free energy, we choose a set of moduli shown in Table 1 to calculate the wave fields at the achiral–chiral interface. Note that the values of λ_2 and μ_2 are measured in reference [4]. The acoustic impedance is then $Z = 1{\cdot}6 \times 10^6\ \text{kg/s m}^2$ and the Poisson's ratio is $v = 0{\cdot}47$.

3. To understand the chirality in the transmitted field, large numerical result and discussions are given in this paper. The numerical results are plotted in polar plots that are very useful in studying the transmission phenomena at an interface. In addition, the transmitted field is more complicated than the reflected field due to the extra mode conversion in the chiral material, while the transmitted field had never been actually solved or mentioned in reference [11]. The power profiles of the transmitted field obtained in this paper reveal that the chirality is enhanced between the first and second transition frequencies. We conclude that the embedded handed microstructures may be properly chosen such that the composite is effectively chiral at a specified frequency range.
4. The energy conservation of the total wave field is derived in our paper. The power profiles in the transmitted field (the chiral medium) would offer a better understanding about chirality. Without that, the wave propagation in the transmitted field is highly obscure.

Furthermore, the mode conversion due to the chirality from the achiral–chiral interface, the coupled phenomena based on the similar wavenumbers of the RCP and LCP plane waves, and the over-determined boundary conditions as mentioned in reference [11], are discussed in detail.

2. CONSTITUTIVE AND WAVE EQUATIONS FOR THE CHIRAL MEDIUM

It is demonstrated that the acoustic wave can also sense the handedness of a chiral medium and an acoustically chiral composite can be constructed by embedding structural chiral microstructures or springs in a host medium [2–4]. The elastodynamic motion of such a material is derived based on the following equations [6, 11]:

conservation of linear momentum:

$$\sigma_{ij,i} + X_j - \rho\ddot{u}_j = 0; \tag{1}$$

conservation of angular momentum:

$$\varepsilon_{jik}\sigma_{ik} + m_{ij,i} + Y_j - J\ddot{\varphi}_j = 0; \tag{2}$$

constitutive equations:

$$\sigma_{ij} = \lambda u_{k,k}\delta_{ij} + \mu(u_{i,j} + u_{j,i}) + C_3\varphi_{j,i}, \tag{3}$$

$$m_{ij} = \alpha\varphi_{k,k}\delta_{ij} + \beta\varphi_{i,j} + \gamma\varphi_{j,i} + C_3u_{j,i} - C_3\varepsilon_{ijk}\varphi_k, \tag{4}$$

where σ_{ij} is the stress tensor, X_j is the body force, ρ is the mass density of the material, u_j is the displacement vector, ε_{jik} is the permutation symbol, m_{ij} is the couple stress tensor, Y_j is the body moment, φ_j is the microrotation vector, J is the polar moment of inertia, λ, μ, α, β, γ, and C_3 are the material moduli, and δ_{ij} is the Kronecker delta. Since the internal energy is non-negative, the following inequalities are modified from reference [14], i.e.,

$$\mu \geqslant 0,\ (3\lambda + 2\mu) \geqslant 0,\ (3\alpha + \beta + \gamma) \geqslant 0,\ \ -\gamma \leqslant \beta \leqslant \gamma,\quad \gamma \geqslant 0,$$

$$C_3^2 \leqslant 8\mu\gamma,\ \frac{C_3^2}{4(3\lambda + 2\mu)(3\alpha + \beta + \gamma)} \leqslant 1. \tag{5}$$

According to the Helmholtz theorem, any vector field can be expressed as the sum of the gradient of a scalar field and the curl of a vector field:

$$\mathbf{u} = \nabla\boldsymbol{\Phi} + \nabla\times\boldsymbol{\psi}, \qquad \nabla\cdot\boldsymbol{\psi} = 0, \tag{6}$$

$$\boldsymbol{\varphi} = \nabla\xi + \nabla\times\mathbf{H}, \qquad \nabla\cdot\mathbf{H} = 0, \tag{7}$$

where $\boldsymbol{\Phi}$, ξ and $\boldsymbol{\psi}$, $\mathbf{H}$ are the scalar and vector potentials respectively. Substitution of equations (6) and (7) into equations (3) and (4) leads to the scalar and vector wave equations respectively. They are

$$(\lambda + 2\mu)\nabla^2\boldsymbol{\Phi} + C_3\nabla^2\xi = \rho\ddot{\boldsymbol{\Phi}}, \tag{8}$$

$$(\alpha + \beta + \gamma)\nabla^2\xi + C_3\nabla^2\boldsymbol{\Phi} = J\rho\ddot{\xi}, \tag{9}$$

$$\mu\nabla^2\boldsymbol{\psi} + C_3\nabla^2\mathbf{H} = \rho\ddot{\boldsymbol{\psi}}, \tag{10}$$

$$\gamma\nabla^2\mathbf{H} + 2C_3\nabla\times\mathbf{H} + C_3\nabla^2\boldsymbol{\psi} = J\rho\ddot{\mathbf{H}}. \tag{11}$$

Most studies about the propagating elastic wave are concerned with an incident harmonic plane wave. The plane wave problems are not only mathematically less complex, but are also a good approximation of many physically meaningful problems. Since this type of incident wave is important, we shall recapitulate the harmonic plane waves propagating in the x–y plane, and may be described as

$$\{\Phi, \xi, \boldsymbol{\psi}, \mathbf{H}\} = \{\Phi^\circ, \xi^\circ, \boldsymbol{\psi}^\circ, \mathbf{H}^\circ\}\exp[\mathrm{i}k(\mathbf{n}\cdot\mathbf{r})]. \tag{12}$$

Here Φ° and ξ° are amplitudes, $\boldsymbol{\psi}^\circ$ and $\mathbf{H}^\circ$ denote the constant vectors, k is the wavenumber, $\mathbf{r}$ is the position vector, and $\mathbf{n}$ indicates a unit vector in the direction of propagation. For brevity in writing it would be assumed, throughout a paper, that it is as a rule to omit the $\exp(-\mathrm{i}\omega t)$ time dependence, where ω is the angular velocity. Substituting equation (12) into equations (8) and (9), one has

$$[(\lambda + 2\mu)(\alpha + \beta + \gamma) - C_3^2]k^4 - \rho\omega^2[J(\lambda + 2\mu) + \alpha + \beta + \gamma]k^2 + J\rho^2\omega^2 = 0. \tag{13}$$

Equation (13) means that there are two sets of coupled non-dispersive longitudinal displacement waves and longitudinal microrotation waves travelling with wavenumbers k_1 and k_2 in the chiral solid. Similarly, by substituting the fields' variables (12) into equations (10) and (11), we obtain the dispersion equation as follows:

$$[(J\rho\omega^2 - k^2\gamma)(\rho\omega^2 - \mu k^2) - C_3^2k^4]^2 - [2C_3k(\mu k^2 - \rho\omega^2)]^2 = 0. \tag{14}$$

The consequence indicates four sets of coupled dispersive transverse displacement waves and transverse microrotation waves travelling with wavenumbers k_3 to k_6, which characterize two sets of the coupled left circularly polarized (LCP) waves and two sets of the coupled right circularly polarized (RCP) waves. Hence, when the plane wave travels on the x–z plane, the coupled RCP and LCP plane waves are given as

$$\mathbf{H}_R = H_R(\mathrm{i}n_1\mathbf{e}_x + \mathbf{e}_y - \mathrm{i}n_3\mathbf{e}_z)\exp[\mathrm{i}k(n_1x + n_3z)], \tag{15}$$

$$\mathbf{H}_L = H_L(-\mathrm{i}n_1\mathbf{e}_x + \mathbf{e}_y + \mathrm{i}n_3\mathbf{e}_z)\exp[\mathrm{i}k(n_1x + n_3z)], \tag{16}$$

In equations (15) and (16), the subscript "R" means the RCP plane wave, "L" denotes the LCP plane wave, and the unit Cartesian vectors have been denoted by $\mathbf{e}_x$, $\mathbf{e}_y$, and $\mathbf{e}_z$. It should be mentioned that the RCP and LCP plane waves propogate in the chiral medium at different phase velocities.

3. WAVE FIELDS FOR ACHIRAL–CHIRAL PROBLEM

For an obliquely incident plane wave, the field representations for the planar two semi-infinite samples can be illustrated by Figure 2. Figure 2 can be divided into two regions: one of them, region $z \leqslant 0$, is an elastic half-space that does not exhibit chirality with the mass density ρ_1, and the *Lame*' constants λ_1 and μ_1. The other one, region $z \geqslant 0$, is a chiral medium (whose elastic parameters are the mass density ρ_2, the polar moment of inertia J, and the material moduli $\lambda_2, \mu_2, \alpha, \beta, \gamma, C_3$). In Figure 2, the SV-wave (vertical shear

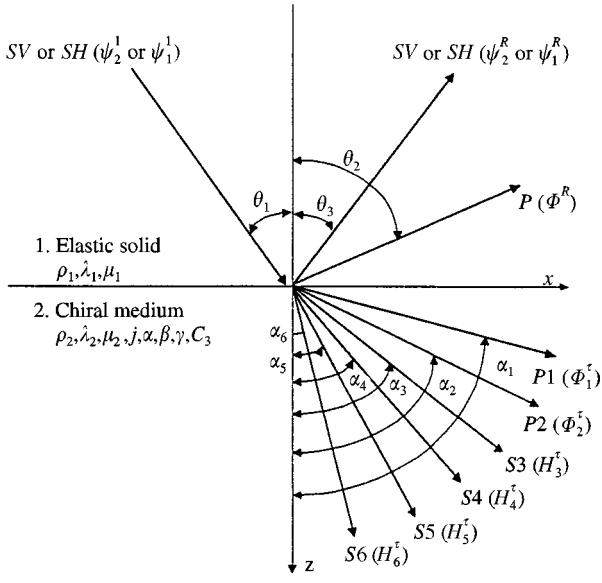

Figure 2. Reflection and transmission of the incident shear plane wave.

wave), and SH-wave (horizontal shear wave) represent the incident and reflected wave types in the elastic (achiral) solid; $P1$ and $P2$ denote the two non-dispersive longitudinal plane waves, and the $S3$, $S4$, $S5$, and $S6$ indicate the four sets of coupled dispersive transverse plane waves in the chiral solid. Hence, consider the incident SV-wave, or SH-wave, the complete problem of reflection and transmission of elastic waves on the interface between an achiral solid and a chiral solid are defined as a series of potential functions of the form given in equations (17)–(23). Consequently, to satisfy the boundary conditions at the interface $z = 0$, the incident transverse (SV or SH) wave of wavenumber k_s at the angle θ_1 with the interface, will result in

(1) a reflected longitudinal displacement wave travelling with wavenumber k_L at an angle of θ_2,
(2) a pair of reflected transverse displacement waves travelling with the same wavenumber k_S at an angle of θ_3,
(3) two transmitted longitudinal displacement waves coupled with the longitudinal microrotational waves travelling with wavenumbers k_1 and k_2 at the angles of α_1 and α_2, respectively, and
(4) four sets of transmitted transverse displacement waves coupled with transverse rotational waves in the angles of α_3 to α_6 at wavenumbers k_3 to k_6 respectively.

Therefore, there are nine unknown coefficients involved in the reflected and transmitted fields. Although the amplitude and direction of the propagating waves are varied in the two media, the wave equations and the boundary conditions at the interface can be satisfied by assuming that the reflected and transmitted waves are still plane waves. Therefore, the incident and reflected plane waves, in general, are given by

$$\boldsymbol{\psi}^{I1} = (\psi_1^I \mathbf{e}_x + \psi_2^I \mathbf{e}_y - \tan\theta_1 \psi_1^I \mathbf{e}_z)\exp[\mathrm{i}k_S(\sin\theta_1 x + \cos\theta_1 z)], \tag{17}$$

$$\Phi^{R1} = \Phi^R \exp[\mathrm{i}k_L(\sin\theta_2 x - \cos\theta_2 z)] \tag{18}$$

and

$$\boldsymbol{\psi}^{R1} = (\psi_1^R \mathbf{e}_x + \psi_2^R \mathbf{e}_y + \tan\theta_3 \psi_1^R \mathbf{e}_z)\exp[\mathrm{i}k_S(\sin\theta_3 x - \cos\theta_3 z)]. \tag{19}$$

Similarly, in the chiral region, the appropriate representations of the field consistent with Snell's laws in the chiral medium are given by

$$\Phi^{T2} = \sum_{q=1}^{2} \Phi_q^R \exp[\mathrm{i}k_q(\sin\alpha_q x + \cos\alpha_q z)], \tag{20}$$

$$\xi^{T2} = \sum_{q=1}^{2} D_q \Phi_q^T \exp[\mathrm{i}k_q \sin\alpha_q x + \cos\alpha_q z)], \tag{21}$$

$$\boldsymbol{\psi}^{T2} = \sum_{q=3}^{6} D_q H_q^T (\Delta_q^1 \mathbf{e}_x + \Delta_q^2 \mathbf{e}_y + \Delta_q^3 \mathbf{e}_z)\exp[\mathrm{i}k_q(\sin\alpha_q x + \cos\alpha_q z)], \tag{22}$$

$$\mathbf{H}^{T2} = \sum_{q=3}^{6} H_q^T (\Delta_q^1 \mathbf{e}_x + \Delta_q^2 \mathbf{e}_y + \Delta_q^3 \mathbf{e}_z)\exp[\mathrm{i}k_q(\sin\alpha_q x + \cos\alpha_q z)]. \tag{23}$$

In these equations, Φ's, H's and ψ's are the amplitudes to be determined by the boundary conditions, and k_L, k_S, and k_q are the wavenumbers of the corresponding waves. For the convenience of the ensuing discussion, the potentials associated with the incident wave are designated by a superscript "$I1$"; those with reflected wave by "RI"; and those with the transmitted waves by "$T2$". It must be mentioned that the formula of D_q can be found in reference [2], i.e.,

$$D_q = \frac{\rho\omega^2 - k_q^2(\lambda_2 + 2\mu_2)}{k_q^2 C_3}, \quad \text{for } q = 1, 2, \tag{24a}$$

and

$$D_q = \frac{k_q^2 C_3}{\rho\omega^2 - \mu_2 k_q^2}, \quad \text{for } q = 3\text{–}6. \tag{24b}$$

The presentation of Δ_q^1, Δ_q^2 and Δ_q^3 is based on equations (15) and (16), and may be written as

$$\Delta_q^1 : \Delta_q^2 : \Delta_q^3 = \pm\mathrm{i}\cos\alpha_q : 1 : \mp\mathrm{i}\sin\alpha_q, \tag{25}$$

in which the upper signs "+" in Δ_q^1 and "−" in Δ_q^3 refer to the RCP plane waves, and the lower signs "−" in Δ_q^1 and "+" in Δ_q^3 to the LCP plane waves.

For a complete description of the problem, nine boundary conditions are needed for solving the nine unknown reflected and transmitted coefficients. Six of the boundary conditions come from the assumption of the continuity for all components of the displacement $\mathbf{u}$ and traction vectors $\boldsymbol{\tau}$ at $z = 0$, i.e.,

$$\mathbf{u}^{I1} + \mathbf{u}^{R1} = \mathbf{u}^{T2}, \tag{26}$$

$$\mathbf{e}_z \cdot (\boldsymbol{\tau}^{I1} + \boldsymbol{\tau}^{R1}) = \mathbf{e}_z \cdot \boldsymbol{\tau}^{T2}. \tag{27}$$

The remaining three conditions may be chosen by considering the continuity of the microrotation and couple stress. Since the difference between the theory of micropolar

elasticity and that of the classical elasticity are the introduction of the microrotation $\boldsymbol{\varphi}$ and couple stress $\mathbf{m}$; therefore, when a wave is propagating at a chiral–chiral interface, both the microrotation and couple stress are continuous at the interface [9, 10]. The microrotation moduli (α, β, γ) and chiral parameter (C_3), however, are null on the achiral surface, so there are no microrotation and couple stress at the achiral–chiral interface [11, 12], i.e.,

$$\boldsymbol{\psi}^{T2} = 0, \tag{28}$$

$$\mathbf{e}_z \cdot \mathbf{m}^{T2} = 0. \tag{29}$$

Only one of the equations (28) or (29) is necessary for the remaining three conditions; otherwise, an over-determined problem will be generated. In the following derivation, we define the boundary conditions A containing equations (26)–(28), as well as boundary conditions **B** to equations (26), (27), and (29). The two sets of conditions shall be discussed separately in this paper. In 1994, Elphinstone [12] reported that the anomalous behavior is influenced by the sets of the boundary conditions used, but none of them resists the principle of conservation of energy. Thus, experimentation is necessary to decide which of the boundary conditions, null of the microrotation or null of the couple stress, is physically relevant in the chiral medium.

Using equations (17)–(23) and the boundary conditions, which leads to a system of nine simultaneous algebraic equations, and can be written as a matrix formula,

$$[E]\{X\} = [F]\{Y\}, \tag{30}$$

where $[E]$ is a 9×9 complex matrix, $[F]$ is a 9×2 matrix, and $\{x\}$, $\{Y\}$ are defined by

$$\{X\} = \{\Phi^R, \psi_1^R, \psi_2^R, \Phi_1^T, \Phi_2^T, H_3^T, H_4^T, H_5^T, H_6^T\}^{\mathrm{T}}, \tag{31}$$

$$\{Y\} = \{\psi_1^I, \psi_2^I\}^{\mathrm{T}} \tag{32}$$

with T^* being *transpose* of the matrix. Hence, $\{Y\}$ contains known incident coefficients, and $\{X\}$ contains three unknown reflected coefficients and six unknown refracted coefficients and six unknown refracted coefficients. For convenience of calculation, the reflected and transmitted coefficients can be explicitly expressed using the relationship $\{X\} = [E]^{-1}[F]\{Y\}$.

In this analysis, there are two special cases of the incident plane-polarized waves in $\{Y\}$ considered here, i.e.,

(1) SV-wave:

$$\psi_2^I = 1, \quad \psi_1^I = 0; \tag{33a}$$

(2) SH-wave:

$$\psi_1^I = 1, \quad \psi_2^I = 0. \tag{33b}$$

Furthermore, equations (17)–(23) satisfy the boundary conditions at $z = 0$, if

$$k_S \sin\theta_1 = k_L \sin\theta_2 = k_S \sin\theta_3 = k_1 \sin\alpha_1 = k_2 \sin\alpha_2 = \cdots, \tag{34}$$

which is the well-known Snell's law.

4. NORMALIZED POWER DENSITIES

We now consider the partitioning of energy between the different reflected and transmitted waves in the achiral–chiral interface. The mechanical power is the product of the surface traction and the particle velocity during displacement and the surface moment and particle velocity during rotation, i.e.,

$$\hat{p} = \sigma_{ij} n_i \dot{u}_j + m_{ij} n_i \dot{\phi}_j. \tag{35}$$

Using equations (17)–(23) and eliminating the remaining time dependence by time averages over the period, the normalized mechanical power density for an incident SV- or SH-wave is given as

$$1 = \frac{\tan\theta_1}{\tan\theta_2}\left(\frac{\Phi^R}{\psi_2^I}\right)^2 + \left[\left(\frac{\psi_2^R}{\psi_2^I}\right)^2 + \left(\frac{\psi_2^R}{\psi_2^I}\right)^2 \sec^2\theta_3\right] + \sum_{q=1}^{2} \frac{k_q^3 \Xi_q^L \cos\alpha_q}{k_S^3 \mu_1 \cos\theta_1}\left(\frac{\Phi_q^T}{\psi_2^I}\right)^2 + \sum_{q=3}^{2} \frac{k_q^3 \Xi_q^S \cos\alpha_q}{k_S^3 \mu_1 \cos\theta_1}\left(\frac{H_q^T}{\psi_2^I}\right)^2, \tag{36}$$

and

$$1 = \frac{\sin\theta_1 \cos\theta_1}{\tan\theta_2}\left(\frac{\Phi^R}{\psi_1^I}\right)^2 + \left[\left(\frac{\psi_2^R}{\psi_1^I}\right)^2 \sec^2\theta_3 + \left(\frac{\psi_2^R}{\psi_1^I}\right)^2\right] + \sum_{q=1}^{2} \frac{k_q^3 \Xi_q^L \cos\alpha_q}{k_S^3 \mu_1 \sec\theta_1}\left(\frac{\Phi_q^T}{\psi_1^I}\right)^2 + \sum_{q=3}^{2} \frac{k_q^3 \Xi_q^S \cos\alpha_q}{k_S^3 \mu_1 \sec\theta_1}\left(\frac{H_q^T}{\psi_1^I}\right)^2, \tag{37}$$

where

$$\Xi_q^L = \lambda_2 + 2\mu_2 + 2C_3 D_4 + (\alpha + \beta + \gamma)(D_q)^2 \tag{38}$$

and

$$\Xi_q^S = 2[\mu_2 (D_q)^2 + \gamma + 2C_3 D_q + \Delta C_3 k_q^{-1}]. \tag{39}$$

Note that the elastic moduli $\{\alpha, \beta, \gamma, C_3\}$ vanish in the medium $z > 0$, and thus the problem reduces to the situation of reflection and transmission from an achiral-achiral interface. With the assumption, the normalized power densities (36) and (37) may reduce to

$$1 = \frac{\tan\theta_1}{\tan\theta_2}\left(\frac{\Phi^R}{\psi_2^I}\right)^2 + \left(\frac{\psi_2^R}{\psi_2^I}\right)^2 + \frac{\rho_2 \tan\theta_1}{\rho_1 \tan\alpha_1}\left(\frac{\Phi^T}{\psi_2^I}\right)^2 + \frac{\rho_2 \tan\theta_1}{\rho_1 \tan\alpha_2}\left(\frac{\psi_2^T}{\psi_2^I}\right)^2 \tag{40}$$

and

$$1 = \left(\frac{\psi_1^R}{\psi_1^I}\right)^2 + \frac{\rho_2 k_{s2} \cos\theta_1}{\rho_1 k_{s1} \cos\theta_2}\left(\frac{\psi_1^T}{\psi_1^I}\right)^2. \tag{41}$$

5. SPECIAL CASE: NORMALLY INCIDENT TRANSVERSE WAVE

We shall here study the field behavior of a normally incident transverse wave at a planar achiral–chiral boundary, i.e., $\theta_1 = 0$. Consider the situation in Figure 1 where the incident plane wave travels in the $+z$ direction, and the boundary surface is in the plane of $z = 0$. Consequently, substituting equations (17)–(23) into the boundary conditions (26) and (27), one obtains

$$k_s\psi_2^R + \sum_{q=3}^{6} D_q k_q H_q^T = k_S\psi_2^I, \tag{42}$$

$$k_s\psi_1^R + \sum_{q=3}^{6} D_q k_q \Delta_q^1 H_q^T = k_S\psi_1^I, \tag{43}$$

$$k_L\Phi^R + \sum_{q=3}^{6} k_q\Phi_q^T = 0, \tag{44}$$

$$-\mu_1 k_S^2\psi_2^R + \sum_{q=3}^{6} k_q^2(\mu_2 D_q + C_3)H_q^T = \mu_1 k_S^2\psi_2^I, \tag{45}$$

$$-\mu_1 k_S^2\psi_1^R + \sum_{q=3}^{6} \Delta_q^1 k_q^2(\mu_2 D_q + C_3)H_q^T = \mu_1 k_S^2\psi_1^I, \tag{46}$$

$$-(\lambda_1 + 2\mu_1)k_L^2\Phi^R + \sum_{q=3}^{6} k_q^2(\lambda_2 + 2\mu_2 + D_q C_3)\Phi_q^T = 0. \tag{47}$$

Similarly, using boundary conditions (28), one obtains

$$\sum_{q=3}^{6} k_q H_q^T = 0, \tag{48}$$

$$\sum_{q=3}^{6} k_q \Delta_q^1 H_q^T = 0, \tag{49}$$

$$\sum_{q=1}^{2} k_q D_q \Phi_q^T = 0, \tag{50}$$

or using conditions (29), one obtains

$$\sum_{q=3}^{6} [k_q^2(\gamma + D_q C_3) - \mathrm{i}C_3 k_q \Delta_q^1] H_q^T = 0, \tag{51}$$

$$\sum_{q=3}^{6} [k_q^2 \Delta_q^1(\gamma + D_q C_3) + \mathrm{i}C_3 k_q] H_q^T = 0, \tag{52}$$

$$\sum_{q=1}^{2} k_q^2[(\alpha + \beta + \gamma)D_q + C_3]\Phi_q^T = 0. \tag{53}$$

For the case of the normally incident transverse wave, equations (44) and (47) together with equations (50) or (53) constitute a homogeneous system of equations of three unknowns. Since the determinate of the coefficient matrix is non-zero, the computations from Cramer's rule [15] imply that

$$\Phi^R = \Phi_1^T = \Phi_2^T = 0. \tag{54}$$

Equation (54) implies that when a transverse plane wave is normally incident at the interface $z = 0$, the longitudinal waves will disappear from media 1 and 2. It means that only the transverse waves exist in the reflected and transmitted fields. Consequently, the normalized power densities are then modified to

$$1 = \left(\frac{\psi_2^R}{\psi_2^I}\right)^2 + \left(\frac{\psi_1^R}{\psi_2^I}\right)^2 + \sum_{q=3}^{6} \frac{\Xi_q^S k_q^3}{\mu_1 k_S^3} \left(\frac{\psi_q^T}{\psi_2^I}\right)^2 \tag{55}$$

and

$$1 = \left(\frac{\psi_{12}^R}{\psi_1^I}\right)^2 + \left(\frac{\psi_2^R}{\psi_1^I}\right)^2 + \sum_{q=3}^{6} \frac{\Xi_q^S k_q^3}{\mu_1 k_S^3} \left(\frac{H_q^T}{\psi_1^I}\right)^2. \tag{56}$$

6. NUMERICAL RESULTS AND DISCUSSION

In order to solve the complete problem of the reflection and transmission of elastic shear waves at the achiral–chiral interface, the material constants of the two specific media listed in Table 1 will be used in the calculation. In the forthcoming section, the following notations are used to represent the reflected and transmitted characteristics:

$$p_{Z,Y}^X, \tag{57}$$

where p is the square root of the normalized power density. In equation (57), $Z = R$ or T denotes the reflected or transmitted field, X and $Y = P$, SV, and SH represent the incident and reflected wave types in the elastic solid, and $Y = \{P1, P2, S3, S4, S5, S6\}$ describes the transmitted wave types in the chiral medium.

In our previous study [2] (see Figure 1), the dispersion equation indicates that there are four dispersive circularly polarized transverse waves propagating in the chiral medium: two RCP plane waves ($S3$ and $S5$) and two LCP plane waves ($S4$ and $S6$), respectively. Notably, the $S4$- and $S5$-waves are close together at frequencies lower than 90 Hz and only three models of the wavenumbers can be found; in the 90 Hz–12 kHz frequency range, four wavenumbers can be found clearly; when the frequency is higher than 12 kHz, $S3$-, $S4$- and $S5$-, $S6$-waves are coupled together, respectively. This observation would lead to different states of the waveforms in the chiral materials. Hence, the two transition frequencies (90 Hz and 12 kHz), properly so called, divide the frequency domain into three groups and the four transverse models can only be distinguished at the specified frequency range. The coupled phenomena mentioned above are also true for wave propagation at the achiral-chiral interface no matter what boundary condition, A or B, is used.

The computed values of the amplitude as functions of the frequency when an SV-wave is normally incident ($\theta_1 = 0$) at the achiral–chiral boundary are shown in Figure 3. From equation (54), it is clear that no longitudinal waves can be found in both the reflected and transmitted fields; therefore, the values of Φ_1^R, Φ_1^T, and Φ_2^T vanish in this figure. Meanwhile, the zero of ψ_1^R as shown in Figure 3 implies the vanishing of the reflected SH-wave in this

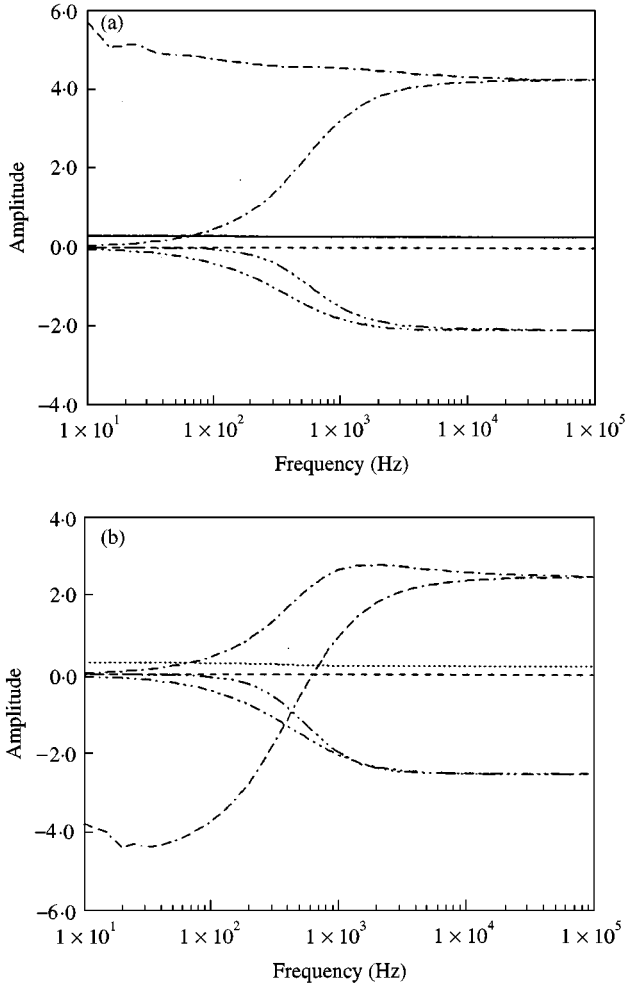

Figure 3. The amplitude ratios of the reflected and transmitted waves as functions of the frequency: (a) boundary conditions A, (b) boundary conditions B. ——, ψ_2^R; – – –, ψ_1^R; – – ·, H_3^T; – · –, H_4^T; – · · –; H_5^T, – · · · –, H_6^T

analysis. The consequence is identical to the classical elasticity: a normally incident SV-wave only results in a reflected SV-wave and hence no mode conversion occurs at the achiral–chiral boundary. Figure 3 also indicates that the profiles of H_4^T, H_5^T, and H_6^T have similar tendencies at boundary conditions A and B: they start from the right-hand side of the figure with the fixed values, and degenerate into two groups: one for H_3^T, H_4^T and the other or H_5^T, H_6^T. In addition, H_4^T, H_5^T, and H_6^T turn into zero at a frequency of 10 Hz. The biggest difference between the two boundary conditions may be the distribution of H_3^T, which has larger value at boundary conditions A, but induces a special characteristic from negative to positive amplitudes at boundary conditions B. Physically, the interesting phenomenon in Figure 3(b) means that H_3^T is 180° out of phase at the value of 630 kHz. The normalized power distributions of the reflected and transmitted waves when an SV-wave is normally incident are plotted in Figure 4. It is observed from Figure 4 that only the power density $p_{R,SV}^{SV}$ exists in the reflected field due to the vanishing of the SH-wave as shown in Figure 3. Meanwhile, the transmitted power densities of the boundary conditions A and B obey the characteristics illustrated in Figure 1. It means that the S4 and S5 modes always

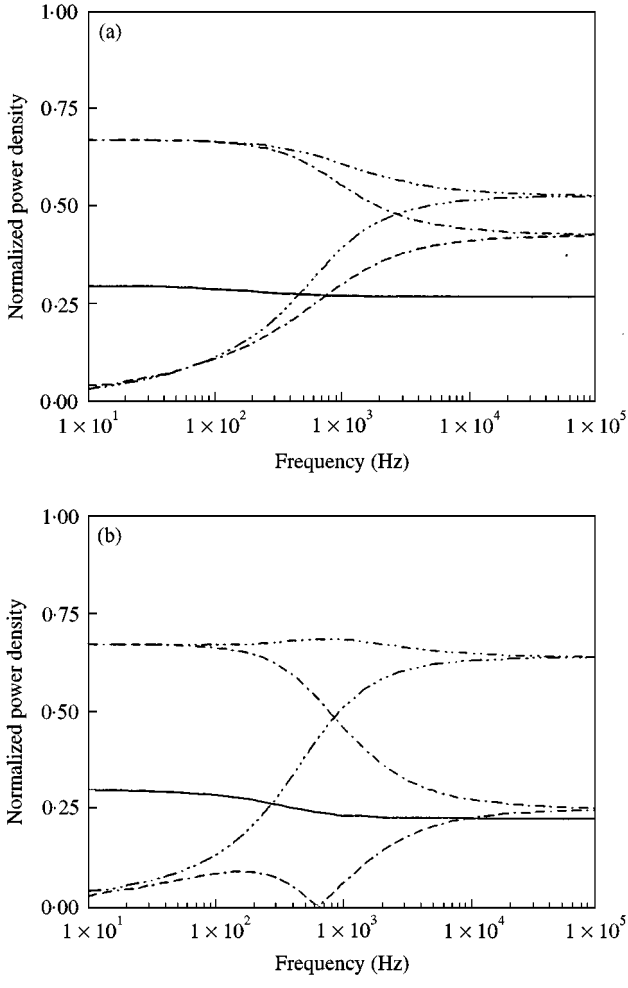

Figure 4. The normalized power densities of the reflected and transmitted waves as functions of the frequency: (a) boundary conditions A, (b) boundary conditions B. ——, $p^{SV}_{R,SV}$; - - -, $p^{SV}_{R,SH}$; – – –, $p^{SV}_{T,S3}$; – · –, $p^{SV}_{T,S4}$; – · · –, $p^{SV}_{T,S5}$; – · · · –, $p^{SV}_{T,S6}$.

couple together and have similar power profiles ($p^{SV}_{T,S4}$ and $p^{SV}_{T,S5}$) at frequencies lower than the first transition frequency; similar power profiles ($p^{SV}_{T,S3}$, $p^{SV}_{T,S4}$ and $p^{SV}_{T,S5}$, $p^{SV}_{T,S6}$) at frequencies higher than the second transition frequency imply the coupled relations of the $S3$, $S4$, and $S5$, $S6$ modes. Furthermore, the characteristic of $S3$-wave travelling from negative to positive values at boundary conditions B implies that the value of $p^{SV}_{T,S3}$ shown in Figure 4(b) is zero at 630 Hz. Also shown in Figure 4(a) and 4(b) is that the power densities of the reflected and transmitted field are dominated by H_4^{T2} and H_5^{T2} at lower frequencies and by H_5^{T2} and H_6^{T2} at higher frequencies.

In examining the direction change of a coupled transverse wave at a given point as t changes, it is convenient to set $z = 0$, and then the transmitted field of a normal incidence can be expressed as

$$\mathbf{H}^{T2}_{3,5} = H^{T}_{3,5}(\mathbf{e}_x \sin \omega t + \mathbf{e}_y \cos \omega t), \tag{58}$$

$$\mathbf{H}^{T2}_{4,6} = H^{T}_{4,6}(-\mathbf{e}_x \sin \omega t + \mathbf{e}_y \cos \omega t). \tag{59}$$

In equations (58) and (59), $\mathbf{H}_3^{T2}$ and $\mathbf{H}_5^{T2}$ are RCP plane waves, and $\mathbf{H}_4^{T2}$ and $\mathbf{H}_6^{T2}$ are LCP plane waves. As ωt increases from 0 through $\pi/2$, π, $3\pi/2$, and a complete cycle of 2π, the tips of the vectors RCP or LCP plane wave will trace a circular locus. As mentioned above, the two circularly polarized waves $\mathbf{H}_4^{T2}$ and $\mathbf{H}_5^{T2}$, due to the characteristic of their similar wavenumbers at the lower frequencies, e.g., 10 Hz (as shown in Figure 1), hence degenerate to a linearly polarized transverse wave propagating in the z direction. Figures 5(a) and 5(b) are specified as the polarization diagram of LCP ($\mathbf{H}_4^{T2}$) and RCP ($\mathbf{H}_5^{T2}$) plane waves respectively, according to equation (58) and (59), and Figure 5(c) is a combination of 5(a) and 5(b), where "s" denotes the starting point. It is observed from Figure 5(c) that the coupled transverse wave oscillates only along the x direction. Similarly, at higher frequencies, e.g., 50 kHz, the RCP ($\mathbf{H}_3^{T2}$) and LCP ($\mathbf{H}_4^{T2}$) plane waves will degenerate to a linearly polarized transverse wave propagating in the z direction. Figures 6(a) and 6(b) represent $\mathbf{H}_3^{T2}$ and $\mathbf{H}_4^{T2}$ respectively, and Figure 6(c) plots the result of 6(a) plus 6(b). Figure 7 is similar to Figure 6 when $\mathbf{H}_3^{T2}$ and $\mathbf{H}_4^{T2}$ are replaced by $\mathbf{H}_5^{T2}$ and $\mathbf{H}_6^{T2}$. Both Figure 6(c) in and 7(c) indicate that the two sets of RCP and LCP plane waves may degenerate to linearly polarized plane waves that always oscillate along the y direction.

It is known that the transverse waves can discriminate the chirality of objects and the characteristics of the two transition frequencies. To further demonstrate the phenomenon, the reflected and transmitted fields of an incident SV-wave are calculated by considering boundary conditions A and plotted in Figures 8 and 9 at 30 Hz, 1 kHz, and 30 kHz. In

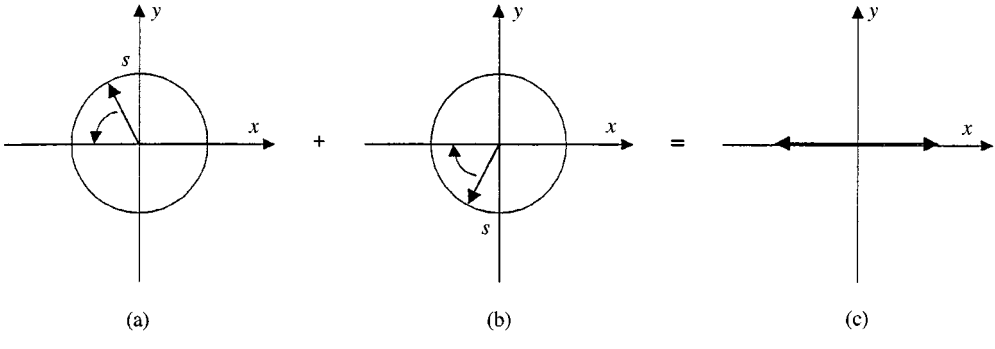

Figure 5. Polarization diagrams for the sum of $\mathbf{H}_4^{T2}$ and $\mathbf{H}_5^{T2}$ in space quadrature at $z = 0$ for $f = 50$ Hz: (a) LCP plane wave ($\mathbf{H}_4^{T2}$), (b) RCP plane wave ($\mathbf{H}_5^{T2}$), (c) a coupled transverses plane wave.

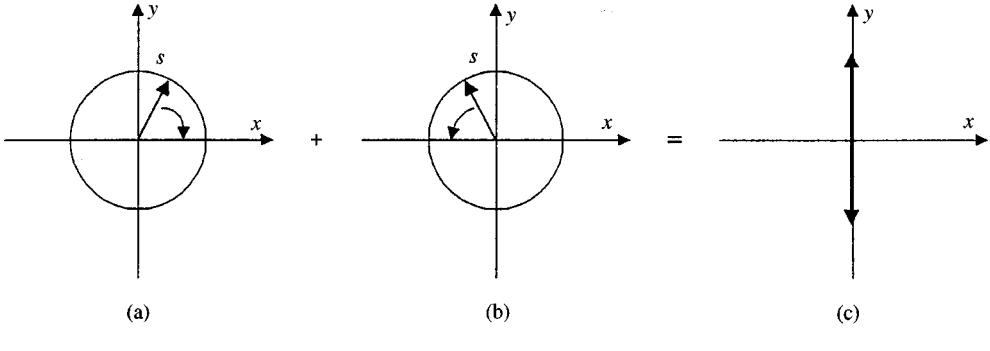

Figure 6. Polarization diagrams for the sum of $\mathbf{H}_3^{T2}$ and $\mathbf{H}_4^{T2}$ in space quadrature at $z = 0$ for $f = 50$ kHz: (a) RCP plane wave ($\mathbf{H}_3^{T2}$), (b) LCP plane wave ($\mathbf{H}_4^{T2}$), (c) a coupled transverse plane wave.

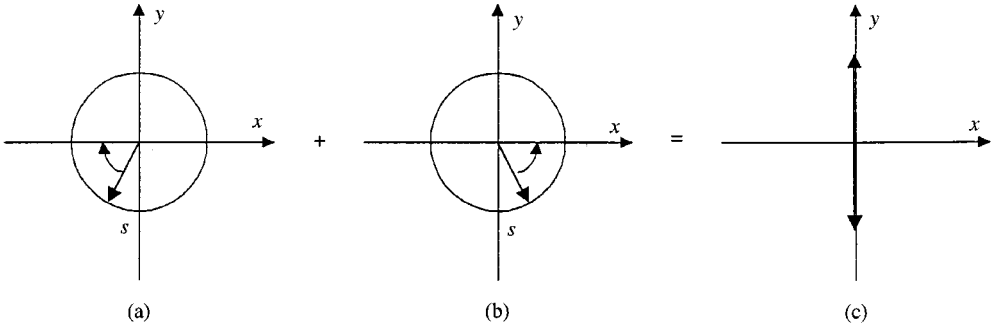

Figure 7. Polarization diagrams for the sum of $\mathbf{H}_5^{T2}$ and $\mathbf{H}_6^{T2}$ in space quadrature at $z = 0$ for $f = 50$ kHz: (a) RCP plane wave ($\mathbf{H}_5^{T2}$), (b) LCP plane wave ($\mathbf{H}_6^{T2}$), (c) a coupled transverse plane wave.

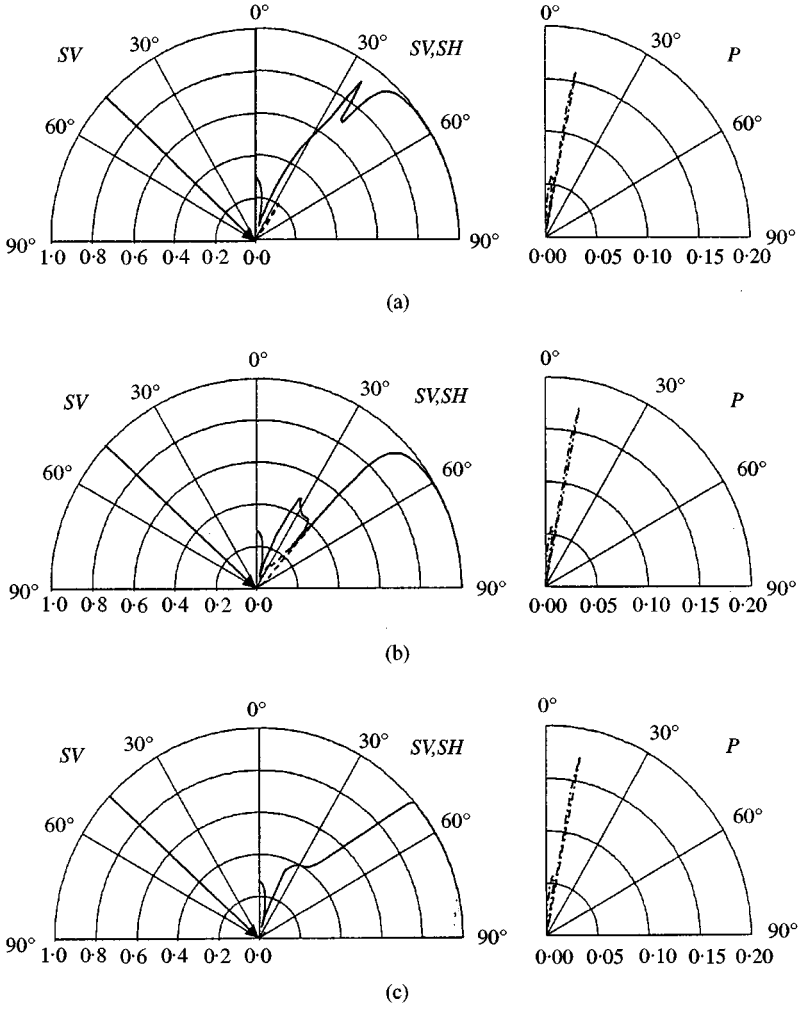

Figure 8. The normalized power densities of the reflected waves for SV-wave incidence at the achiral–chiral boundary. The boundary conditions A are used for: (a) 30 Hz, (b) 1 kHz, (c) 30 kHz. ——, $p_{R,SV}^{SV}$; - - -, $p_{R,SH}^{SV}$; – · –, $p_{R,P}^{SV}$.

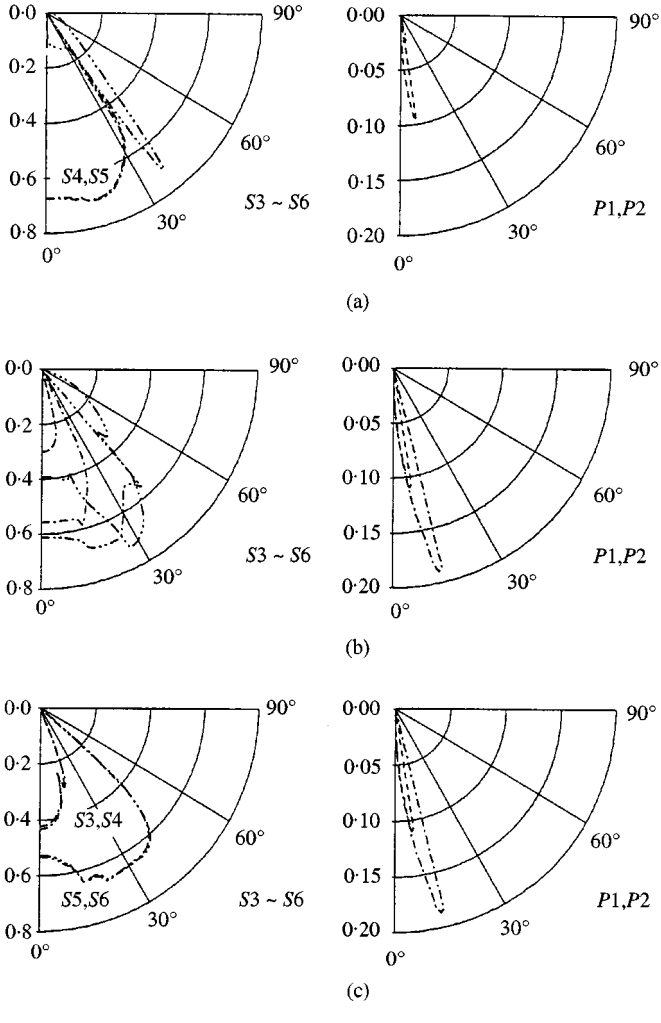

Figure 9. The normalized power densities of the transmitted waves for SV-wave incidence at the achiral–chiral boundary. The boundary conditions A are used for: (a) 30 Hz, (b) 1 kHz, (c) 30 kHz. Left column: – – · –, $p^{SV}_{T,S3}$; – · –, $p^{SV}_{T,S4}$; – · · · –, $p^{SV}_{T,S5}$; – · · · –, $p^{SV}_{T,S6}$. Right column: - - -, $p^{SV}_{T,P1}$; – · –, $p^{SV}_{T,P2}$.

Figure 8, the first and second quadrants of the plots on the left denote the incident SV-waves and the reflected shear waves (SV- and SH-waves), and the plots on the right are the reflected longitudinal wave (*P*-wave). Also in Figure 9, the plots on the left represent the transmitted transverse waves (S3- to S6-waves), an the plots on the right describe the transmitted longitudinal waves (*P*1- and P2-waves). All the power densities in polar plot are functions of the incident angle. It is observed that the trend of the reflected power-density profiles (i.e., $p^{SV}_{R,SV}$, $p^{SV}_{R,SH}$, and $p^{SV}_{R,P}$ shown in Figure 8) is the same for the three specified frequencies if the incident angle is lower than 22°. From the profiles, evidently the $p^{SV}_{R,SV}$ starts with a fixed value when $\theta_1 = 0°$; as θ_1 increases, it diminishes at $\theta_1 = 9°$ and 14·8° due to the grazing transmitted *P*1- and *P*2-waves. In addition, the $p^{SV}_{R,SV}$ profile changes its value dramatically at 33·9° for 30 Hz, 26 and 42° for 1 kHz, and 22 and 48° for 30 kHz, which are called Rayleigh-wood anomalies [16] due to the grazing transmitted *S*4- and *S*5-waves (see the left column plotted in Figure 9). It means that the *S*4- and *S*5-waves become an evanescent wave and decay exponentially into the interior half-space. The

phenomenon leads to a redistribution of the power densities of the reflected and transmitted plane waves that are still propagating. Consequently, the $p^{SV}_{R,SV}$ profiles seem to reach the maximum, respectively, right after the Rayleigh-wood anomalies. This simply means that more energy goes into the reflected SV-wave. In view of the case of incident SV-wave, due to the chirality in medium 2, the existence of SH-waves is observed. This important phenomenon does not appear in the classic elastic solid. Note that the $p^{SV}_{R,SH}$ at 1 kHz is the largest among the three cases in Figure 8. Also, the transmitted transverse waves display the same phenomena shown in Figure 4, i.e., below the first transition frequency, the $S4$- and $S5$-waves have similar wavenumbers and hence the $p^{SV}_{T,S4}$ and $p^{SV}_{T,S5}$ simultaneously possess similar powers. In between the first and second transition frequencies, the four circularly transverse waves are evidently distinguished, which induce the variable power-density profiles in it. When the frequency is higher than the second transition frequency, the $S3$-, $S4$- and $S5$-, $S6$-waves would degenerate into the new transverse waves, which implies the similar power densities $p^{SV}_{T,S3}$, $p^{SV}_{T,S4}$ and $p^{SV}_{T,S5}$, $p^{SV}_{T,S6}$, respectively. Moreover, the grazing angles of $S4$- and $S5$-waves in Figures 9(a) and 9(b) would induce the redistribution of the reflected power densities. Hence the $p^{SV}_{R,SH}$ has the maximum if one of the Rayleigh-wood anomalies due to the evanescent $S4$- and $S5$-waves occurs.

Figure 10 plots the power density of the reflected and transmitted fields for an obliquely incident SV-wave. The boundary conditions B are considered in this calculation. The first and second quadrants of the plots on the left denote the incident and reflected shear waves, the fourth quadrant of the plots on the left represents the transmitted transverse waves, the first quadrant of the plots on the right is the reflected longitudinal wave, and the fourth quadrant of the plots on the right describes the transmitted longitudinal waves. In Figure 10, the reflected and transmitted longitudinal fields are similar to Figures 8 and 9, except that the $p^{SV}_{T,PZ}$ profiles are different. Moreover, the SH-wave, according to the mode conversion of the chirality, again appears in this case. Identical to the conclusion mentioned in Figure 9(b), the power density $p^{SV}_{T,SH}$ is again superior at a frequency of 1 kHz. These numerical results also indicate that the use of boundary conditions B obtains a greater effect of chirality than the use of boundary conditions A (see the profiles of $p^{SV}_{T,SH}$ shown in Figures 9(b) and 10(b)). Although the two types of boundary conditions, A and B, always display variable numerical computations, they are in agreement with the principle of conservation of energy. The consequence of using either boundary conditions A or B is confusing because only one of the boundary conditions A or B is specified at a point on the interface in all physical problems [17]. Aero *et al.* [5], in a study on the continuum theory of asymmetric elasticity, indicate that when the two semi-infinite media are in contact and no interaction exists between the particles at the boundary zone, it is natural to assume the continuity of the microrotation. They also reported that the free energy of the chiral solid must reach a minimum when it is in a state of stable dynamic equilibrium. Accordingly, the boundary conditions A are a better choice than conditions B among the first and second transition frequencies, and will be used in the following analysis.

To further illustrate the effects of the chirality, the chiral half-space is replaced by an isotropic (achiral) material. The transmitted field hence contains only three material constants $\{\lambda_2, \mu_2, \rho_2\}$ listed in Table 1, and the numerical results are plotted in Figure 11. When compared with Figures 8–10, it is clear that the existence of the chirality in medium 2 would instigate a reducible power density $p^{SV}_{R,SV}$. Hence, the largest discrepancy in the achiral–achiral and achiral–chiral cases may occur at 1 kHz, or at any frequencies lying between the first and second transition frequencies.

Since the value of C_3 leads to a distinct phenomenon of chirality [2], the variety of C_3 is another interesting issue in this analysis. Shown in Figure 12 is the power-density profiles of the two cases: (a) $C_3 = 4 \times 10^6$ N/m and (b) $C_3 = 35 \times 10^6$ N/m respectively. Since the

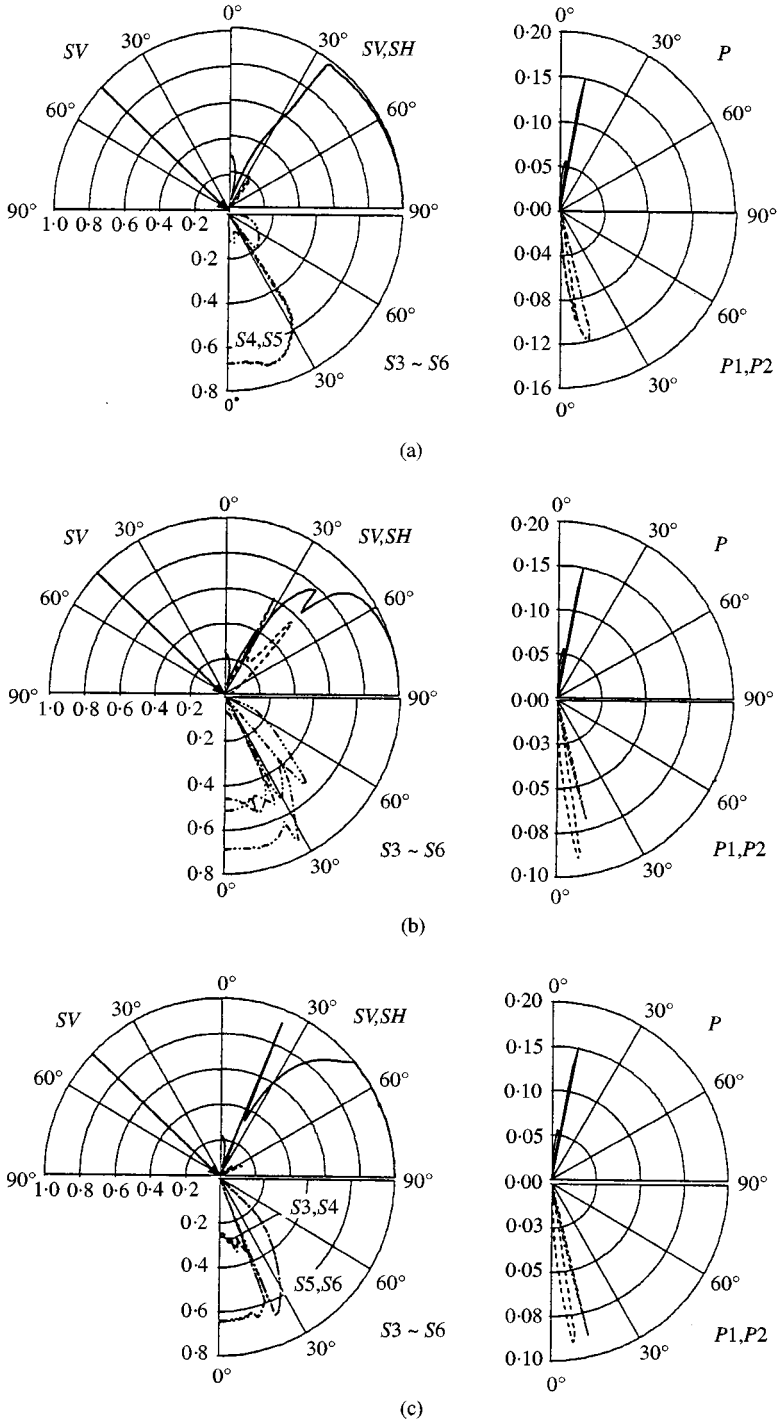

Figure 10. The normalized power densities of the incident SV-wave at the achiral–chiral boundary. The boundary conditions B are used for: (a) 30 Hz, (b) 1 kHz, (c) 30 kHz. Left column: ——, $p^{SV}_{R,SV}$; - - -, $p^{SV}_{R,SH}$; – – –, $p^{SV}_{T,S3}$; – · –, $p^{SV}_{T,S4}$; – · · · –, $p^{SV}_{T,S5}$; – · · · · –, $p^{SV}_{T,S6}$. Right column: – · –, $p^{SV}_{R,P}$; - - -, $p^{SV}_{T,P1}$; – · –, $p^{SV}_{T,P2}$.

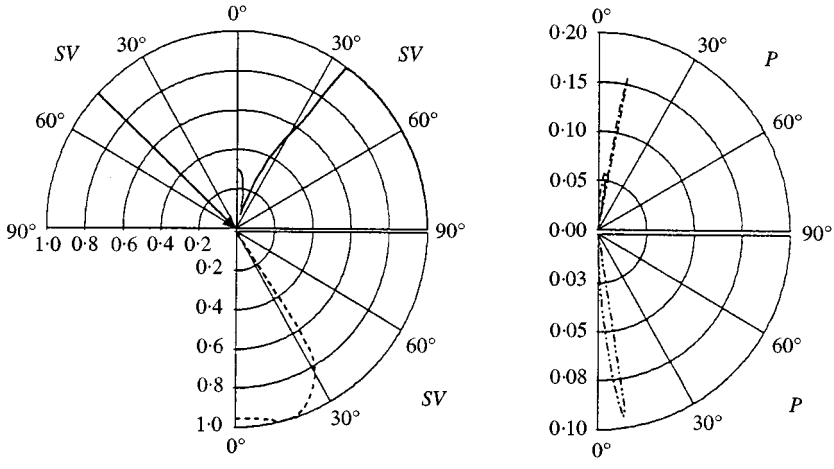

Figure 11. The normalized power densities of the incident SV-wave in elastic solid against achiral medium that the properties used are only the ρ_2, λ_2, and μ_2 in Table 1. ——, $p^{SV}_{R,SV}$; - - -, $p^{SV}_{T,SV}$; – · –, $p^{SV}_{R,P}$; – · · · –, $p^{SV}_{T,P}$.

influence of chirality on medium 2 is enhanced at 1 kHz, these figures are all plotted based on the calculation using this frequency. It is observed that the reflected field in Figure 12(a) is similar to the achiral–achiral case (shown in Figure 11). This reveals the general insensitivity of $p^{SV}_{R,P}$ and $p^{SV}_{R,SV}$ to the chiral parameter C_3 if the value of C_3 is small. Also, the numerical results indicate that the trend of the power density $p^{SV}_{T,S5}$ and $p^{SV}_{T,S6}$ is similar in the fourth quadrant of the plot on the left-hand side that simultaneously possesses the major power density in the transmitted field. When C_3 increases, e.g., $C_3 = 26 \times 10^6$ N/m, the $p^{SV}_{R,SH}$ is smaller but expands to a wider region when compared to Figures 8(b) and 10(b). Hence, only a suitable choice of C_3 can induce a better chiral effect on the chiral medium.

The reflected and transmitted phenomena of the incident SH-wave at the achiral–chiral interface are plotted in Figure 13. Again, it is interesting to observe the existence of P- and SV-waves due to the effect of chirality. The numerical analysis also indicates that the value of $p^{SV}_{R,SV}$ is the largest at 1 kHz among the three specific frequencies (the cases of 30 Hz and 30 kHz are not shown in this figure). We then concluded that, when the frequency of the incident wave lies in the frequency range where four circularly polarized shear waves are found, the conversion of the power density due to the mode conversion is the largest. Consequently, the P-, SV-, and SH-waves are coupled together and should be considered in the wave propagation at the achiral–chiral interface.

Until now, only the linear polarized incident plane wave is discussed. From Figures 3 and 4, it is known that the normally incident SV-wave may reflect an SV-wave in the zone of $z < 0$ from the achiral–chiral interface. Consequently, the reflected SH-wave is absent; therefore, there is no mode conversion from the achiral–chiral interface in this case. To study the behavior of chirality in detail, we now consider either a normally incident RCP or LCP plane wave at the interface $z = 0$. It will be appropriate to express the incident field by the forms

(1) RCP plane wave:

$$\psi_1^I = \mathrm{i}, \quad \psi_2^I = 1; \tag{60}$$

(2) LCP plane wave:

$$\psi_1^I = -\mathrm{i}, \quad \psi_2^I = 1. \tag{61}$$

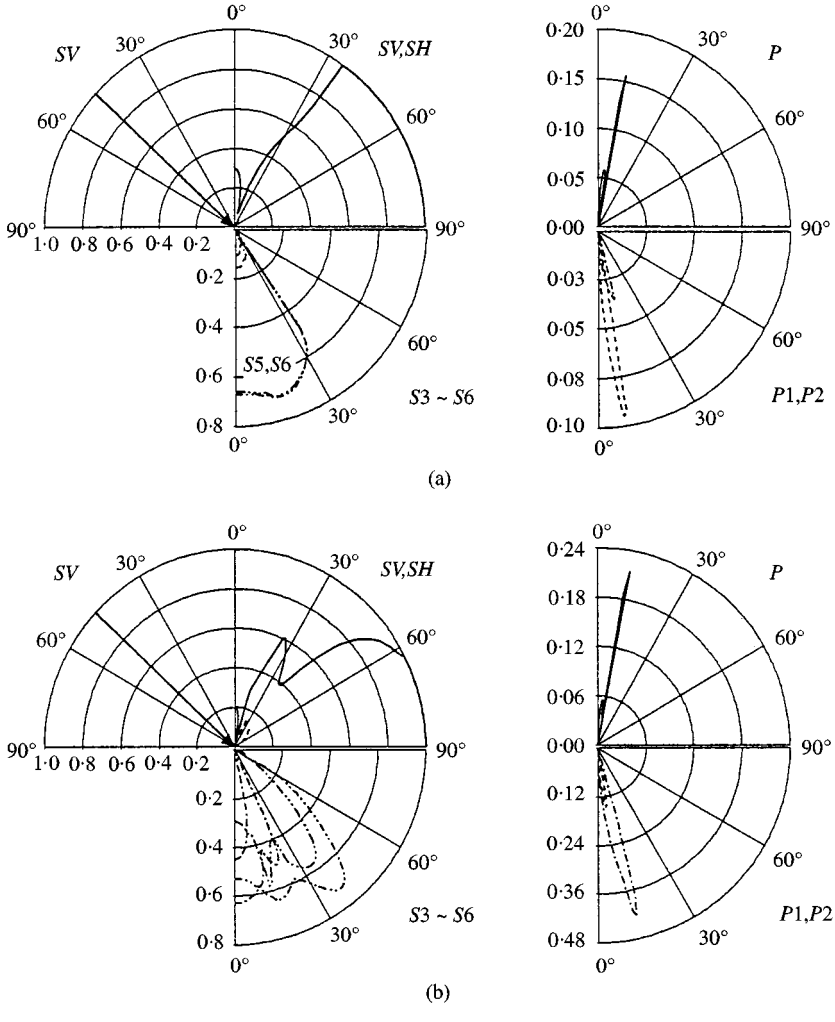

Figure 12. The normalized power densities of the incident SV-wave at achiral–chiral interface for (a) $C_3 = 3 \times 10^6$ N/m or (b) $C_3 = 26 \times 10^6$ N/m. Left column: ——, $p^{SV}_{R,SV}$; - - -, $p^{SV}_{R,SH}$; — - —, $p^{SV}_{T,S3}$; — · —, $p^{SV}_{T,S4}$; — · · —, $p^{SV}_{T,S5}$; — · · · —, $p^{SV}_{T,S6}$. Right column: ——, $p^{SV}_{R,P}$; - - -, $p^{SV}_{T,P1}$; — · —, $p^{SV}_{T,P2}$.

The solution of the boundary value problem is plotted in Figure 14. Figure 14 indicates that if the incident plane wave is RCP, then the transmitted waves are also RCP. However, to satisfy the boundary conditions, the reflected wave must be LCP. The result is also true for the incident LCP plane wave that it generates a reflected RCP plane wave and two transmitted LCP plane waves from the achiral–chiral interface. Therefore, we conclude that the reflected field of the chiral medium is linearly polarized for a normally incident, linearly polarized wave; whereas the normally incident, circularly polarized wave cause a reflected wave with circular polarization along the z axis but oscillates in the reverse direction of rotation.

7. CONCLUSIONS

A theoretical analysis has been conducted in detail to understand the phenomena of the transverse wave propagating at the achiral–chiral interface. Using a series of wave equations and the appropriate boundary conditions, the reflected and transmitted

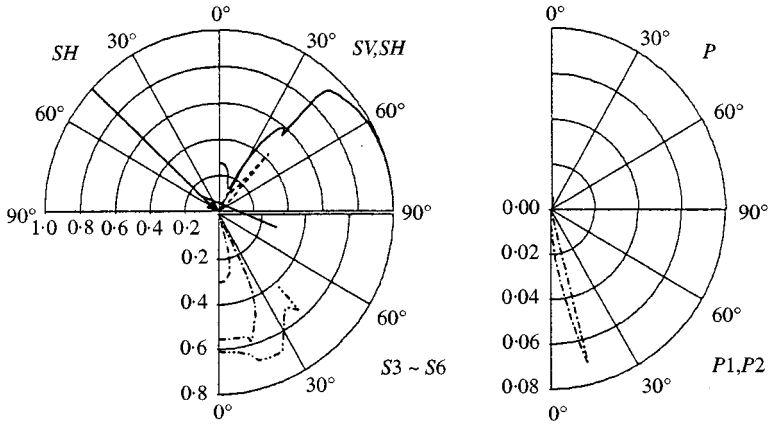

Figure 13. The normalized power densities of the incident SH-wave at the achiral–chiral boundary for 1 kHz. Left column: ——, $p^{SH}_{R,SH}$; - - -, $p^{SH}_{R,SV}$; – – ·, $p^{SH}_{T,S3}$; – · –, $p^{SH}_{T,S4}$; – · · –, $p^{SH}_{T,S5}$; – · · · –, $p^{SH}_{T,S6}$. Right column: ——, $p^{SH}_{R,P}$; - - -, $p^{SH}_{T,P1}$; – · –, $p^{SH}_{T,P2}$.

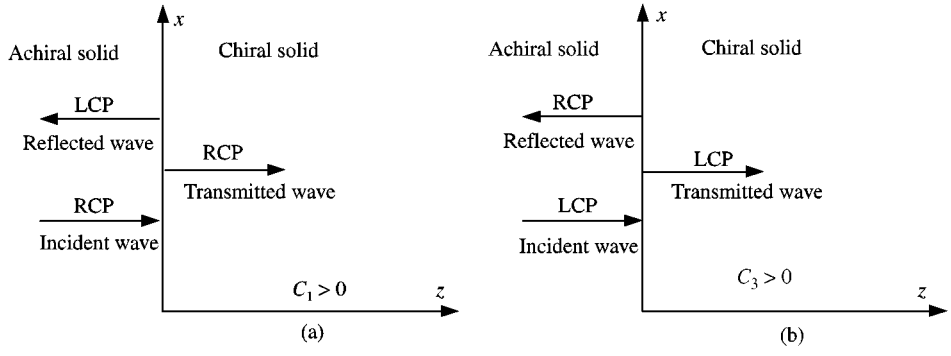

Figure 14. Field represents for the normal incidences: (a) RCP plane wave, (b) LCP plane wave.

characteristics can be solved numerically, and the solutions are in agreement with the principle of conservation of energy. The results have shown that for a normally incident, linearly polarized shear wave, there is no mode conversion due to the handedness of the chiral property. It means that an incident SV-wave will generate a reflected SV-wave as well as four transverse waves, i.e., *S*3- to *S*6-waves, whereas the longitudinal waves would disappear in this case. Also, the coupled transverse waves (RCP and LCP) propagating in the chiral medium may degenerate to a linearly transverse wave oscillating along a unique direction. If the oblique incidence is concerned, the reflected and transmitted power densities are shown in the polar diagrams at 30 Hz, 1 kHz, and 30 kHz respectively. We then concluded that the *P*- SV-, and SH-waves are coupled together due to the existence of chirality, and simultaneously, the phenomenon is particularly enhanced between the first and second transition frequencies.

ACKNOWLEDGMENTS

This investigation was supported in part by the National Science Council of Taiwan, Republic of China, through the grant NSC 86-2212-E-110-001.

REFERENCES

1. J. APPLEQUIST 1987 *American Scientist* **75**, 59–68. Optical activity: Biot's bequest.
2. S. K. YANG and S. Y. HSIA 1995 *Proceedings of the 8th Asia-Pacific Conference NDT*, 303–309. Wave propagation in effective chiral composites (I) the characteristics of dispersion equations.
3. S. K. YANG, V. V. VARADAN, A. LAKHTAKIA and V. K. VARADAN 1991 *Journal of Physics D: Applied Physics* **24**, 1601–1608. Reflection and transmission of elastic waves by a structurally chiral arrangement of identical uniaxial layers.
4. V. V. VARADN, S. K. YANG and V. K. VARADAN 1992 *Journal of Sound and Vibration* **159**, 403–420. Rotation of elastic shear waves in laminated, structurally chiral composites.
5. E. L. AERO and E. V. KUVSHINSKII 1065 *Physics of Solids* **6**, 2141–2148. Continuum theory of asymmetric elasticity equilibrium of an isotropic body.
6. A. C. ERINGEN 1968 *Fracture I*. (H. Liebowitz; editor) Academic, New York.
7. W. NOWACKI 1986 *Theory of Asymmetric Elasticity*. Pergamon Press: Oxford.
8. V. R. PARFITT 1969 *Journal of the Acoustical Society of America* **45**, 1258–1272. Reflection of plane waves from the flat boundary of a micropolar elastic half-space.
9. S. K. TOMAR and M. L. GOGNA 1992 *International Journal of Engineering Science* **30**, 1637–1646. Reflection and refraction of a longitudinal microrotational wave at an interface between two micropolar elastic solids in welded contact.
10. S. K. TOMAR 1995 *Journal of Acoustical Society of America* **97**, 822–830. Reflection and refraction of a longitudinal wave at an interface between two micropolar elastic solids in welded contact.
11. A. LAKHTAKIA, V. K. VARADAN and V. V. VARADAN 1990 *Journal of the Acoustical Society of America* **83**, 2314–2318. Reflection of elastic plane waves at a planar achiral–chiral interface.
12. M. J. ELPHINSTONE and A. LAKHTAKIA 1994 *Journal of the Acoustical Society of America* **95**, 617–627. Plane-wave response of an elastic chiral solid slab sandwiched between achiral solid half-spaces.
13. L. E. KINSLER, A. R. FREY, A. B. COPPENS and J. V. SANDERS 1982 *Fundamentals of Acoustics*. John Wiley & Sons: New York.
14. R. . LAKES and R. L. BENEDICT 1982 *International Journal of Engineering Science* **20**, 1161–1167. Noncentrosymmetry in micropolar elasticity.
15. C. R. WYLIE and L. C. BARRETT 1982 *Advanced Engineering Mathematics*. McGraw-Hill, Inc.: New York.
16. A. LAKHTAKIA, V. K. VARADAN and V. V. VARADAN 1985 *Journal of Applied Mechanics* **52**, 144–148. The acoustic response of a periodically rough elastic plate (ice) in contact with water.
17. J. N. REDDY and M. L. RASMUSSEN 1982 *Advanced Engineering Analysis*. John Wiley & Sons; New York.